

Cite this: *Soft Matter*, 2011, **7**, 6092

www.rsc.org/softmatter

PAPER

## Vesicles with multiple membrane domains†

Jinglei Hu,\* Thomas Weikl and Reinhard Lipowsky

Received 16th December 2010, Accepted 4th April 2011

DOI: 10.1039/c0sm01500h

Vesicles with two types of intramembrane domains, both of which are in the fluid state, are studied theoretically using free energy minimization and Monte Carlo simulations. Specific examples are provided by liquid-ordered and liquid-disordered domains, which are formed by phase separation within multi-component membranes. Multi-domain morphologies, which arise from the interplay between the bending energies of the domains and the line energy of the domain boundaries, are found for a wide range of these elastic parameters and can be further stabilized by the constraint of constant volume, by spontaneous curvatures, and/or by a difference in the Gaussian curvature moduli of the two types of domains. In the latter case, the vesicles attain stable multi-domain morphologies with up to six liquid-disordered domains. Morphologies with three and four such domains have also been observed experimentally, in qualitative agreement with our simulations. For sufficiently small line tension, “lipid rafts” with multiple liquid-ordered domains are also found to be stable if the liquid-ordered domains have a positive spontaneous curvature. The vesicles are found to undergo a variety of transitions between different multi-domain morphologies. Presumably the simplest way to explore these morphological transitions experimentally is by changing the vesicle volume *via* osmotic deflation.

### 1 Introduction

In the context of liquid droplets, the tension of the contact line, which was already considered by Gibbs, represents a relatively small correction term to the interfacial free energies.<sup>1</sup> Therefore, this line tension hardly affects the morphology of micrometer-sized droplets. In contrast, the line tension associated with intramembrane domains, which was introduced and first discussed in ref. 2, has a rather strong effect on the shape of membranes and vesicles. Indeed, the line tension can deform the membrane shape as predicted theoretically<sup>2,3</sup> and confirmed experimentally by optical microscopy of giant vesicles.<sup>4–8</sup> The vesicle membranes studied in these experiments contained three components, a saturated lipid such as sphingomyelin, an unsaturated phospholipid, and cholesterol, corresponding to “raft” mixtures that have been postulated to lead to lipid domains in biological membranes.<sup>9</sup> For certain lipid compositions, these membranes undergo phase separation *via* the formation of liquid-ordered ( $\mathcal{L}_o$ ) and liquid-disordered ( $\mathcal{L}_d$ ) domains.

During the initial stage of such a phase separation process, many small domains are formed which then grow and merge into larger domains, a process that can be studied by computer simulations of small vesicles<sup>10</sup> and by optical microscopy of large vesicles.<sup>11</sup> Naïvely, one would expect that this coarsening process

leads to a final state with only two large domains. It has been recently found, however, that domain patterns with more than two domains may also represent stable equilibrium states of such a vesicle.<sup>12</sup> The latter results were obtained by minimization of the vesicle’s configurational energy, a method that neglects all fluctuations of the membrane shape and of the intramembrane domains. In the present paper, we will include all of these fluctuations by studying the vesicle’s morphology *via* Monte Carlo simulations.

The results of our simulations are illustrated in Fig. 1, which displays vesicle morphologies with three and four flexible  $\mathcal{L}_d$  domains within a single  $\mathcal{L}_o$  domain. In this figure, both morphologies, as obtained in our simulations, are compared with those observed experimentally in ref. 11 and 13. The simulated morphologies exhibit both fluctuations of the vesicle shape and fluctuations of the domain boundaries as visible in Fig. 1(a) and 1(c) but the overall domain patterns were very stable. Close inspection of the two morphologies reveals that this stability arises from the arrangement of the more flexible  $\mathcal{L}_d$  domains, which occupy the more strongly curved regions of the vesicle shape and allow the more rigid  $\mathcal{L}_o$  domains to bend only weakly.

We will determine the dependence of the vesicle morphologies and domain patterns both on the elastic membrane parameters and on certain experimentally accessible control parameters. The most important elastic parameters are the bending rigidities of the two intramembrane domains and the line tension of the domain boundaries. In addition, we will also study the influence of the Gaussian curvature moduli and the spontaneous (or preferred) curvatures of the membrane domains. Important

Department of Theory and Bio-Systems, Max Planck Institute of Colloids and Interfaces, 14424 Potsdam, Germany. E-mail: jinglei.hu@mpikg.mpg.de; lipowsky@mpikg.mpg.de

† Electronic supplementary information (ESI) available. See DOI: 10.1039/c0sm01500h

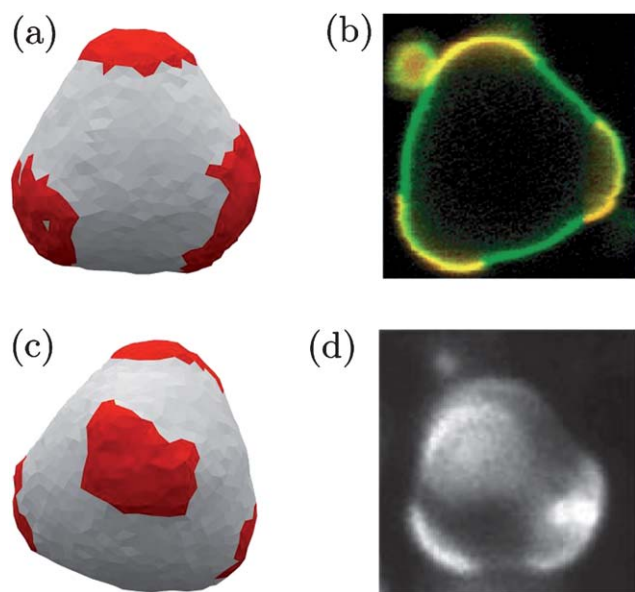


**Fig. 1** Comparison of vesicle morphologies as obtained from our Monte Carlo simulations and observed by optical microscopy.<sup>11,13</sup> In all four subfigures, the majority phase corresponds to the more rigid  $\mathcal{L}_o$  phase, also denoted by  $\alpha$ , which forms a single, multiply-connected domain, whereas the more flexible minority phase  $\mathcal{L}_d$  or  $\beta$  phase forms three or four disconnected domains. In the Monte Carlo snapshots (a) and (c), the more flexible  $\mathcal{L}_d$  domains are shown in red, the more rigid  $\mathcal{L}_o$  domain in light grey. (a) Monte Carlo snapshot for membrane composition  $\chi^{(\alpha)} = 0.6$ , bending rigidity ratio  $\kappa^{(\alpha)}/\kappa^{(\beta)} = 6.0$  and reduced volume  $v = 0.94$ ; (b) fluorescence microscopy image for ESM/*trans*-DOPC/*cis*-DOPC/cholesterol, adopted from ref. 13 (ESM = egg sphingomyelin, DOPC = dioleoyl-phosphatidylcholine, DMPC = dimyristoyl-phosphatidylcholine); (c) Monte Carlo snapshot for  $\chi^{(\alpha)} = 0.7$ ,  $\kappa^{(\alpha)}/\kappa^{(\beta)} = 6.0$  and  $v = 0.92$ ; and (d) phase contrast microscopy image from ref. 11 for 1 : 1 DOPC/DMPC + 30% cholesterol.

control parameters are provided by the membrane composition, the membrane surface area, and the vesicle volume. The variation of these parameters leads to morphological transitions, at which certain patterns of intramembrane domains are transformed into completely different patterns. These transitions are only possible since both types of domains are fluid. Indeed, solid-like domains have a frozen shape and a certain pattern of such domains cannot be transformed into another pattern without first melting these domains.

Our article is organized as follows. In Sec. 2, the continuum description for multicomponent vesicles is briefly reviewed and then mapped onto a discretized description that can be studied by simulations. In contrast to previous simulation studies, we include the Gaussian curvature terms in the discretized bending energy. The flat configurations of the discretized membrane are equivalent to the Ising model on a honeycomb lattice, for which we use the exact result for the line tension in order to relate the results of the Monte Carlo simulations and those of the numerical energy minimization. In Sec. 3, we first describe the competition between this line tension and the two bending rigidities of the two types of membrane domains. We construct the morphology diagrams of the vesicles as a function of membrane composition and other system parameters including the reduced vesicle volume. Two types of novel domain patterns

are found. First, several of the more rigid  $\mathcal{L}_o$  domains can form a stable pattern within a single  $\mathcal{L}_d$  domain when the  $\mathcal{L}_o$  domains have a positive spontaneous curvature. Furthermore, a difference in the Gaussian curvature modulus is shown to induce stable morphologies with up to six of the more flexible  $\mathcal{L}_d$  domains within a single  $\mathcal{L}_o$  domain.

## 2 Theoretical description and methods

### 2.1 Continuum theory of multicomponent vesicles

First, we briefly review the continuum theory of multicomponent vesicles developed by Jülicher and Lipowsky in ref. 3 and 14, in which the membrane is treated as an elastic sheet. In this theory, one simply starts from a multicomponent vesicle with two well-separated fluid phases. As mentioned in the introduction, one example is provided by the liquid-ordered ( $\mathcal{L}_o$ ) and the liquid-disordered ( $\mathcal{L}_d$ ) phase. In order to emphasize that our theory is completely general, we will also use the generic notation  $\alpha$  and  $\beta$  for  $\mathcal{L}_o$  and  $\mathcal{L}_d$ , respectively. Within the  $\alpha$  and  $\beta$  phases, the compositions are assumed to be homogeneous. Taking the mass conservation of lipid molecules constituting the two phases into account as well as the experimental findings that the energetic cost to change the area per lipid molecules is as high as  $50\text{--}100 T \text{ nm}^{-2}$ ,<sup>15</sup> where  $T$  denotes the thermal energy at room temperature, the total domain areas  $A^{(\alpha)}$  and  $A^{(\beta)}$  can be considered to be essentially fixed. The total energy of the vesicle can then be expressed as<sup>3,14</sup>

$$\mathcal{E} = \mathcal{E}_{bc}^{(\alpha)} + \mathcal{E}_{bc}^{(\beta)} + \lambda^{(\alpha,\beta)} \int_{\partial S} dl + \Sigma^{(\alpha)} A^{(\alpha)} + \Sigma^{(\beta)} A^{(\beta)} + PV \quad (1)$$

with the bending energy<sup>16</sup>

$$\mathcal{E}_{bc}^{(i)} \equiv \int_i dA [2\kappa^{(i)}(M - m^{(i)})^2 + \kappa_G^{(i)}G]. \quad (2)$$

The superscript  $i$  refers to the  $\alpha$  or  $\beta$  membrane patches, the symbols  $M$  and  $G$  denote the mean curvature and the Gaussian curvature on the membrane surface. For homogeneous domains, the bending modulus  $\kappa^{(i)}$ , and the Gaussian modulus  $\kappa_G^{(i)}$  as well as the spontaneous curvatures  $m^{(i)}$  are constants. If we take  $\kappa_G^{(\alpha)} = \kappa_G^{(\beta)}$ , the contribution from the Gaussian curvature in eqn (2) would be  $4\pi\kappa_G^{(\alpha)}$  according to the Gauss–Bonnet theorem in differential geometry.<sup>17</sup> Thus, the Gaussian curvature does not affect the vesicle morphology when both phases have the same Gaussian curvature modulus.

In eqn (1), the third term arising from the line tension  $\lambda^{(\alpha,\beta)}$  involves the integral along the domain boundaries  $\partial S$ . The Lagrange multipliers  $\Sigma^{(\alpha)}$  and  $\Sigma^{(\beta)}$  are introduced to enforce the area constraints as stated above.  $P$  is the osmotic pressure for the enclosed volume  $V$  of the vesicle due to the concentration difference of osmotically active molecules between the inside and the outside of the vesicle.

The theory provides a framework within which the shape equation can be numerically solved for axisymmetric shapes as produced by multicomponent vesicles with two well-separated domains. For vesicles with more than two domains, the vesicle shapes and morphologies are, in general, non-axisymmetric and have to be studied by numerical minimization and simulation methods. In fact, for more than two domains, energy minimization methods are somewhat limited since they require an

educated guess about the number of the domains and their relative sizes. In contrast, the Monte Carlo method as described in the next section determines both the number and the relative sizes of the domains without any “prejudice”.

## 2.2 Monte Carlo simulation

In Monte Carlo (MC) simulations, the vesicle is discretized into a triangulated surface with two different types of triangles,  $\alpha$  and  $\beta$ , corresponding to the rigid and flexible membrane patches. Simulations with molecular models of membranes indicate that the whole spectrum of bending deformations is captured if the linear patch size is around 5 nm.<sup>18</sup> The vesicle configurations are changed using three MC moves: (i) the vertices of the triangles are randomly translated to mimic the thermally-excited shape fluctuation; (ii) the edges of adjacent triangles are flipped to describe the fluidity within the membrane; and (iii)  $\alpha$  and  $\beta$  triangles are exchanged to facilitate domain formation and coarsening. In the original implementation of the dynamic MC scheme,<sup>10</sup> only nearest neighboring pairs of  $\alpha$  and  $\beta$  triangles were swapped in order to study the phase separation dynamics. Since we are primarily interested in the thermodynamical stability of different phase structures, we allow global exchange of different triangles but ensure detailed balance at each exchange step.

In order to preserve the connectivity of the whole surface, any two vertices shared by one common edge interact through a tether potential with a tether length of  $\sqrt{3}l_{\text{hc}}$ ,<sup>19</sup> where  $l_{\text{hc}}$  denotes the hard-core diameter. For this potential, tether lengths between  $l_{\text{hc}}$  and  $\sqrt{3}l_{\text{hc}}$  have the same energy, while other lengths would have an infinite energy and are, thus, suppressed in the simulations. In canonical ensemble MC, the probability distribution for the configuration is given by the Boltzmann factor  $e^{-\mathcal{H}_{\text{eff}}/T}$ , where  $T$  is the temperature in energy units and the configurational energy or effective “Hamiltonian”  $\mathcal{H}_{\text{eff}}$  has the form

$$\mathcal{H}_{\text{eff}} = \mathcal{H}_{\text{te}} + \mathcal{H}_{\text{be}} + \mathcal{H}_{\text{in}} \quad (3)$$

corresponding to the tether potentials, the bending energies and the mutual interactions between neighboring membrane patches.

**2.2.1 Bending energy of membrane shape.** For the triangulated surface, the bending energy  $\mathcal{H}_{\text{be}}$  is a sum over the contribution of each triangle  $I$ . For each triangle  $I$ , the integrated mean curvature  $(AM)_I$  over its area  $A_I$  is given by<sup>10,20</sup>

$$(AM)_I = \frac{1}{4} \sum_J l_{IJ} \theta_{IJ} \quad (4)$$

which sums the contribution from  $I$ 's three nearest neighboring triangles. The parameter  $l_{IJ}$  is the length of the edge shared by  $I$  and its neighbor  $J$ , and the tilt angle  $\theta_{IJ}$  describes the angle between the normal vectors of triangles  $I$  and  $J$ .<sup>‡</sup> Thus, a large tilt angle  $\theta_{IJ}$  between the triangles  $I$  and  $J$  implies a large mean curvature. We also define the discretized spontaneous curvature

$(Am)_I$  as the integral of the spontaneous curvature in eqn (2) over the triangle area  $A_I$  which leads to the expression

$$(Am)_I \equiv m^{(I)} A_I \quad (5)$$

with  $m^{(I)}$  being either  $m^{(\alpha)}$  or  $m^{(\beta)}$ . It now follows from the Gauss–Bonnet theorem, when applied to the discrete triangulated surface, that the integral of the Gaussian curvature  $G$  over the whole surface is given by<sup>21,22</sup>

$$\int dAG = \sum_i \left( 2\pi - \sum_I \phi_I \right), \quad (6)$$

where the sum runs over all the vertices  $i$  and  $\phi_I$  is the angle of the adjacent triangle  $I$  at the vertex  $i$ .  $(2\pi - \sum_I \phi_I)$  in eqn (6) is often called the “angle deflection”<sup>22</sup> or “angle deficit”<sup>23</sup> in computational geometry. We note that eqn (6) is consistent with Descartes’ theorem on the total angle deficit of a polyhedron which states that the sum of angle deflections is  $4\pi$  for any polyhedron with the topology of a sphere.<sup>23</sup> Indeed, the integral on the left-hand side of eqn (6) is also equal to  $4\pi$  for any shape that has the topology of a sphere. A detailed derivation of Descartes’ theorem can be found in ref. 22. The local Gaussian curvature  $(AG)_i$  associated with vertex  $i$  is then defined via

$$(AG)_i \equiv \int_{A_i} dAG = 2\pi - \sum_I \phi_I, \quad (7)$$

where the area  $A_i$  associated with vertex  $i$  is related to the areas of the adjacent triangles by

$$A_i \equiv \frac{1}{3} \sum_I A_I. \quad (8)$$

The factor of 1/3 takes into account that three vertices share one triangle. Using eqn (7) and eqn (8), we define the integrated Gaussian curvature  $(AG)_I$  for each triangle  $I$  as

$$(AG)_I = \frac{A_I}{3} \sum_i (AG)_i / A_i. \quad (9)$$

Here the sum runs over the three vertices  $i$  of triangle  $I$ . Note that eqn (9) ensures  $\sum_I (AG)_I = \sum_i (AG)_i$ , i.e., the sums of the Gaussian curvature terms over all triangles and over all vertices are equal, satisfying the Gauss–Bonnet theorem in eqn (6).

To summarize, the discrete bending energy is taken to be

$$\mathcal{H}_{\text{be}} = \sum_I \left\{ 2\kappa^{(I)} [(AM)_I - (Am)_I]^2 / A_I + \kappa_G^{(I)} (AG)_I \right\} \quad (10)$$

with the bending modulus  $\kappa^{(I)}$  and the Gaussian modulus  $\kappa_G^{(I)}$  for triangle  $I$ .

**2.2.2 Interaction energy of membrane patches.** The interaction energy is given by

$$\mathcal{H}_{\text{in}} = \sum_{\langle IJ \rangle} U_{IJ} \quad (11)$$

where the sum runs over all nearest neighbor pairs  $IJ$  and  $U_{IJ}$  denotes the corresponding interaction energy for each  $IJ$  pair. Eqn (11) can be rewritten as

<sup>‡</sup> In ref. 10, the angle  $\theta_{IJ}$  was expressed as  $\arccos(\hat{e}_I \cdot \hat{e}_J)$  where  $\hat{e}_I$  and  $\hat{e}_J$  are the normal vectors of triangle  $I$  and  $J$ , respectively. This expression should be complemented by a sign check.

$$\mathcal{H}_{\text{in}} = N_{\alpha\alpha}U_{\alpha\alpha} + N_{\beta\beta}U_{\beta\beta} + N_{\alpha\beta}U_{\alpha\beta} \quad (12)$$

where  $N_{\alpha\alpha}$  denotes the number of edges between two  $\alpha$  triangles, *etc.* For a given vesicle, the total numbers of  $\alpha$  and  $\beta$  triangles,  $N_t^{(\alpha)}$  and  $N_t^{(\beta)}$ , satisfy

$$3N_t^{(\alpha)} = 2N_{\alpha\alpha} + N_{\alpha\beta} \quad (13)$$

and

$$3N_t^{(\beta)} = 2N_{\beta\beta} + N_{\alpha\beta}, \quad (14)$$

respectively. The coordination number 3 again takes into account that each triangle has three nearest neighbor triangles, which are either  $\alpha$  or  $\beta$ . Using eqn (13) and eqn (14), the interaction energy in eqn (12) now becomes

$$\mathcal{H}_{\text{in}} = N_{\alpha\beta} \left[ U_{\alpha\beta} - \frac{1}{2}(U_{\alpha\alpha} + U_{\beta\beta}) \right] + \frac{3}{2} \left[ N_t^{(\alpha)} U_{\alpha\alpha} + N_t^{(\beta)} U_{\beta\beta} \right]. \quad (15)$$

The last term on the right-hand side of eqn (15) represents a constant energy term independent of the domain pattern on a vesicle with fixed composition and, thus, does not affect the vesicle morphology. Therefore, we define the interaction parameter  $U$  as

$$U \equiv U_{\alpha\beta} - \frac{1}{2}(U_{\alpha\alpha} + U_{\beta\beta}), \quad (16)$$

and use positive values of  $U$  to describe effectively repulsive interactions between the  $\alpha$  and  $\beta$  patches. The interaction energy now has the rather simple form

$$\mathcal{H}_{\text{in}} = N_{\alpha\beta}U \quad (17)$$

which is proportional to the number of edges  $N_{\alpha\beta}$  between two different types of triangles, *i.e.*, one  $\alpha$  and one  $\beta$  triangle.

The flat configuration of the discretized surface is equivalent to the Ising model on a honeycomb lattice with coordination number  $z = 3$ . If  $\kappa^{(\alpha)} = \kappa^{(\beta)}$ , the configurations will be independent of the bending moduli because the bending curvature energies are then invariant under  $\alpha\beta$  exchange. Through the transformation from the Ising model to the binary mixture model, the interaction parameter  $U$  used for MC simulations is given by  $U = 2J$ , where  $J$  is the well-known spin-spin interaction parameter in the Ising model. The exact solution for the Ising model on a honeycomb lattice with coordination number  $z = 3$  gives the critical value<sup>24</sup>  $J_c/T = 0.5 \ln(2 + \sqrt{3})$  which implies the critical value

$$U_c = T \ln(2 + \sqrt{3}) \quad (18)$$

for the interaction parameter  $U$ . This value provides a rough estimate for the critical point of the multicomponent vesicle discretized as a triangulated surface. Theoretical calculations<sup>25</sup> and MC simulations<sup>26</sup> indicate that the critical value is not shifted by membrane shape fluctuations, since local fluctuations in mean curvature are not correlated for unbound membranes.

In practice, one can also decide about the presence or absence of phase separation for a multicomponent vesicle with given material parameters and compositions by visual inspection of the morphological evolution in the MC simulations. For all simulations described below, we used interaction parameters  $U > U_c$ ,

for which the two-component membrane undergoes phase separation.

**2.2.3 Constraints on membrane area and volume.** To compare with real vesicles, one also needs to consider area conservation of the  $\alpha$  and  $\beta$  domains. We use the additional harmonic energy term<sup>27</sup>

$$\mathcal{H}_{\text{area}} = K^{(\alpha)} \left[ 1 - A^{(\alpha)}/A_0^{(\alpha)} \right]^2 + K^{(\beta)} \left[ 1 - A^{(\beta)}/A_0^{(\beta)} \right]^2 \quad (19)$$

to constrain the total areas for both  $\alpha$  and  $\beta$  triangles. Here, the total triangle areas  $A^{(\alpha)}$  and  $A^{(\beta)}$  are defined by

$$A^{(\alpha)} = \sum_I^{(\alpha)} A_I \quad (20)$$

and

$$A^{(\beta)} = \sum_I^{(\beta)} A_I, \quad (21)$$

where the sums run over all the  $\alpha$  and  $\beta$  triangles, respectively. In eqn (19), the areas  $A_0^{(\alpha)}$  and  $A_0^{(\beta)}$  represent the preset values of the constrained areas  $A^{(\alpha)}$  and  $A^{(\beta)}$ . The parameters  $K^{(\alpha)}$  and  $K^{(\beta)}$  are analogous to the area compression moduli and affect the MC simulations *via* the Boltzmann factor  $e^{-\mathcal{H}/T}$  in the reduced and dimensionless form  $K^{(\alpha)}/T$  and  $K^{(\beta)}/T$ . In practise, the values of these dimensionless parameters were chosen to be of the order  $10^6$  in order to ensure that the relative area changes for the equilibrated vesicles are less than 0.1%, *i.e.*,  $|A^{(i)} - A_0^{(i)}|/A_0^{(i)} < 10^{-3}$  for  $i = \alpha, \beta$ .

As mentioned before, the osmotic pressure also imposes a volume constraint on the vesicle which leads to the osmotic energy term<sup>28,29</sup>

$$E_{\text{os}} \approx \frac{T\rho_{\text{ex}}V_{\text{os}}}{2} \left( \frac{V - V_{\text{os}}}{V_{\text{os}}} \right)^2 \quad (22)$$

for small deviations  $(V - V_{\text{os}})/V_{\text{os}}$ . The density  $\rho_{\text{ex}}$  is the particle number per unit volume of the osmotically active molecules outside the vesicle,  $V_{\text{os}} \equiv N_{\text{in}}/\rho_{\text{ex}}$  is the volume, at which the osmotic pressure vanishes, and  $N_{\text{in}}$  is the number of the active molecules enclosed by the vesicle volume  $V$ . In the MC simulations, we use the energy form

$$\mathcal{H}_{\text{vol}} = K_{\text{os}}(1 - V/V_{\text{os}})^2 \quad (23)$$

to account for the harmonic constraint on the vesicle volume. The Boltzmann factor and, thus, the MC configurations depend only on the reduced parameter  $K_{\text{os}}/T$ , which was chosen to be  $K_{\text{os}}/T = 2 \times 10^5$  in order to ensure that the volume fluctuations  $|1 - V/V_{\text{os}}|$  around the preset volume  $V_{\text{os}}$  are smaller than 0.5% for the equilibrated vesicle. The absence of the volume constraint, on the other hand, corresponds to the choice  $K_{\text{os}} = 0$ .

In the MC simulations described below, we will use the effective Hamiltonian  $\mathcal{H}_{\text{eff}}$  as in eqn (3) together with the harmonic constraints given by eqn (19) and eqn (23).

### 2.3 Numerical energy minimization

In our MC simulations, the number and arrangement of the intramembrane domains arise from the relaxation of the vesicle towards equilibrium. Because  $\alpha$  and  $\beta$  patches are continuously

exchanged during the simulations, a given domain may break up into two separate ones and two domains may coalesce into a single one. As a consequence, we do not have to start the simulations from a certain initial domain pattern, even though we can reduce the equilibration time if this initial pattern is close to the one in equilibrium. In contrast, in order to minimize the vesicle energy numerically, we need to (i) choose a certain number of minority phase domains and (ii) allocate a certain membrane area to each of these domains. The vesicle energy is then minimized in the morphology subspace that is characterized by a fixed number of minority phase domains and fixed areas of these domains.

In the MC simulations, the domain boundaries undergo strong shape fluctuations. In contrast, when the vesicle energy is numerically minimized, we have to consider the average shape of the domain boundaries, which are then governed by the line tension  $\lambda^{(\alpha,\beta)}$ . In order to obtain a relation between this line tension and the interaction parameter  $U$  of the membrane patches in the MC simulations, we use the exact solution of the Ising model on the honeycomb lattice as given by eqn (15) in ref. 30. As a result, the line tension  $\lambda^{(\alpha,\beta)}$  is given by

$$\lambda^{(\alpha,\beta)} = \frac{2T}{l_c} \left( u - \ln \left[ \frac{1 + \sqrt{4s^2 + 1}}{2s} \right] \right) \quad (24)$$

with the average length  $l_c$  of the edges forming the phase boundaries and the dimensionless parameters

$$u \equiv U/2T \text{ and } s \equiv \sinh(U/2T). \quad (25)$$

The numerical energy minimization is done as in ref. 12 with the help of the public domain software ‘‘Surface Evolver’’.<sup>31</sup> The initial triangulated surface is minimized *via* gradient descent iterations. To validate our numerical scheme, we take the following steps to check whether we get minimal energy: (i) perturb the already minimized vesicle by, *e.g.*, a bending rigidity change; (ii) minimize the perturbed surface until the relative energy change is smaller than a small threshold value, say 1%; (iii) release the perturbation and minimize the surface again. All the numerical minimization calculations reported in this paper were characterized by a relative energy change  $2|E_1 - E_2|/(E_1 + E_2) < 1\%$  and a relative volume change  $2|V_1 - V_2|/(V_1 + V_2) < 1\%$  for vesicles without volume constraint, where the subscripts 1 and 2 denote the states before and after the perturbation, respectively.

## 2.4 Dimensionless parameters

The overall vesicle geometry can be characterized by its average area  $A_0$  and its average volume  $V_{os}$ . It will be convenient to measure all length scales in units of the vesicle size

$$R_0 \equiv \sqrt{A_0/4\pi} \quad (26)$$

and to introduce the reduced volume

$$v \equiv \frac{V_{os}}{(4\pi/3)R_0^3} \leq 1. \quad (27)$$

The size  $R_0$  represents the radius of a sphere with area  $A_0$  corresponding to the limiting value  $v = 1$  for the reduced volume.

For a phase separated membrane, the total membrane area  $A_0$  can be divided up into the area  $A^{(\alpha)}$  of all  $\alpha$  domains and the area  $A^{(\beta)}$  of all  $\beta$  domains with  $A_0 = A^{(\alpha)} + A^{(\beta)}$ . The molecular composition of the membrane can then be characterized by the area fraction  $\chi^{(\alpha)}$  of the  $\alpha$  domains as defined by

$$\chi^{(\alpha)} \equiv \frac{A_0^{(\alpha)}}{A_0^{(\alpha)} + A_0^{(\beta)}}. \quad (28)$$

The configurational energy or effective ‘‘Hamiltonian’’ of the vesicle depends on the bending rigidities  $\kappa^{(\alpha)}$  and  $\kappa^{(\beta)}$ , on the difference or contrast

$$\Delta\kappa_G \equiv \kappa_G^{(\alpha)} - \kappa_G^{(\beta)} \quad (29)$$

of the Gaussian curvature moduli  $\kappa_G^{(\alpha)}$  and  $\kappa_G^{(\beta)}$ , on the spontaneous curvatures  $m^{(\alpha)}$  and  $m^{(\beta)}$ , and on the line tension  $\lambda^{(\alpha,\beta)}$ . In order to reduce the number of parameters, we will take  $\kappa^{(\beta)}$  as the basic energy scale and describe the elastic properties in terms of the dimensionless bending rigidities  $\kappa^{(\alpha)}/\kappa^{(\beta)}$  as well as the dimensionless difference  $\Delta\kappa_G/\kappa^{(\beta)}$  of the Gaussian curvature moduli.

Likewise, we will use the basic length scale  $R_0$  and the basic energy scale  $\kappa^{(\beta)}$  to define the dimensionless spontaneous curvatures  $m^{(\alpha)}R_0$  and  $m^{(\beta)}R_0$  as well as the dimensionless line tension

$$\lambda \equiv \frac{\lambda^{(\alpha,\beta)}R_0}{\kappa^{(\beta)}}. \quad (30)$$

In the MC simulations, the Boltzmann factor  $e^{-\mathcal{F}/T}$  depends on the dimensionless parameters  $\kappa^{(\alpha)}/T$ ,  $\kappa_G^{(\alpha)}/T$ , and  $U/T$  with the interaction parameter  $U$  as given by eqn (16). In all our simulations, the bending rigidity of the  $\beta$  phase was taken to have the fixed value  $\kappa^{(\beta)} = 10T$ , as appropriate for a flexible phospholipid membrane at room temperature, whereas the bending rigidity  $\kappa^{(\alpha)} = (\kappa^{(\alpha)}/\kappa^{(\beta)})10T$  and the contrast  $\Delta\kappa_G = (\Delta\kappa_G/\kappa^{(\beta)})10T$  were varied over a certain range by changing the ratios  $\kappa^{(\alpha)}/\kappa^{(\beta)}$  and  $\Delta\kappa_G/\kappa^{(\beta)}$ , respectively.

The dimensionless interaction parameter  $U/T$  determines the line tension  $\lambda^{(\alpha,\beta)}$  as described by eqn (24) and (25). Most of our simulations were performed for  $U = 2U_c$ . In addition, we also explored the range  $1.2U_c \leq U \leq 2U_c$ . All of these  $U$ -values exceed the critical value  $U_c$  and, thus, correspond to phase separated membranes.

## 3 Results and discussion

We follow the notation  $\mathcal{A}_B$  as introduced in ref. 12 to describe the domain patterns of the phase separated vesicle. The Roman numeral  $\mathcal{A} = \text{I, II, III, ...}$  corresponds to the number of the relatively rigid  $\alpha$  or liquid-ordered ( $\mathcal{L}_o$ ) domains, and the Arabic subscript  $B = 1, 2, 3, ...$  denotes the number of the relatively flexible  $\beta$  or liquid-disordered ( $\mathcal{L}_d$ ) domains.<sup>§</sup>

### 3.1 Multiple $\mathcal{L}_d$ domains stabilized by bending energy

The simplest case corresponds to vesicles that can freely adapt their volume and are characterized by vanishing spontaneous

<sup>§</sup> The coloring for the two types of phases as used here are, however, different from the one used in ref. 12

curvatures as well as by identical Gaussian curvature moduli for the two types of domains. In this case, the vesicle morphologies depend only on the area fraction  $\chi^{(\alpha)}$  of the  $\alpha$  or liquid-ordered domains, the bending rigidities  $\kappa^{(\alpha)}$  and  $\kappa^{(\beta)}$ , as well as on the line tension  $\lambda^{(\alpha,\beta)}$ . The corresponding morphology diagram is shown in Fig. 2(a) as a function of area fraction  $\chi^{(\alpha)}$  and bending rigidity ratio  $\kappa^{(\alpha)}/\kappa^{(\beta)}$  for dimensionless line tension  $\lambda = 1.67$ . The latter value of  $\lambda$  corresponds to the interaction parameter  $U = 2U_c$  as follows from eqn (24) and eqn (30) with the critical value  $U_c$  as given by eqn (18).

The different morphologies shown in Fig. 2 arise from the competition between bending rigidities and line tension. For relatively small values  $\kappa^{(\alpha)}/\kappa^{(\beta)} \lesssim 3$ , the vesicle attains the I<sub>1</sub> morphology to minimize the dominant line tension energy between the two phases. For larger values  $\kappa^{(\alpha)}/\kappa^{(\beta)} \gtrsim 7$ , one encounters either the I<sub>1</sub> or the II<sub>1</sub> morphologies, for which the rigid  $\alpha$  domains are fairly planar to minimize the dominant bending energy, see the II<sub>1</sub> morphology in Fig. 2(b). For intermediate values of  $\kappa^{(\alpha)}/\kappa^{(\beta)}$ , vesicles with  $\chi^{(\alpha)} < 0.5$ , for which the  $\alpha$  or liquid-ordered phase corresponds to the minority phase, are found to attain either I<sub>1</sub> or II<sub>1</sub> morphologies. Vesicles with  $\chi^{(\alpha)} >$

0.5, on the other hand, exhibit morphologies with multiple  $\beta$  or liquid-disordered domains, see the I<sub>2</sub>, I<sub>3</sub> and I<sub>4</sub> morphologies in Fig. 2(b). Very similar morphology diagrams are also found for smaller line tensions as shown in Figs. S1 and S2†.

For area fraction  $\chi^{(\alpha)} < 1/2$  and large rigidity  $\kappa^{(\alpha)}$  of the more rigid  $\alpha$  phase, the vesicle undergoes a morphological transition from the I<sub>1</sub> morphology with one  $\alpha$  domain to the II<sub>1</sub> morphologies with two  $\alpha$  domains, see Fig. 2(a). The existence of this morphological transition can be intuitively understood as follows. For a very rigid  $\alpha$  phase, *i.e.*, for large  $\kappa^{(\alpha)}$ , the  $\alpha$  domain attains a planar shape. If the area  $A_0^{(\alpha)}$  of the  $\alpha$  phase is small compared to the area  $A_0^{(\beta)}$  of the  $\beta$  phase, *i.e.*, in the limit of small  $\chi^{(\alpha)}$ , the  $\alpha$  phase will form a single, planar domain in order to minimize the line energy of the  $\alpha\beta$  domain boundary, and the  $\beta$  phase will form a large, near-spherical cap with a small planar base provided by the  $\alpha$  domain, corresponding to the I<sub>1</sub> morphology. The latter morphology will persist as we start to increase the area  $A_0^{(\alpha)}$  of the planar  $\alpha$  domain, but it can do so only up to  $A_0^{(\alpha)} = A_0^{(\beta)}$  or  $\chi^{(\alpha)} = 1/2$ . In the latter case, the  $\beta$  domain becomes planar as well. For  $\chi^{(\alpha)} > 1/2$ , the I<sub>1</sub> morphology is no longer possible, and the  $\alpha$  phase has to form two planar  $\alpha$  domains in order to accommodate the minority  $\beta$  phase. As a consequence, the vesicle attains the II<sub>1</sub> morphology for a very rigid  $\alpha$  phase and  $\chi^{(\alpha)} > 1/2$ . Therefore, the vesicle must undergo a morphological transition from I<sub>1</sub> to II<sub>1</sub> as we increase the area fraction  $\chi^{(\alpha)}$  from  $\chi^{(\alpha)} = 0$  to  $\chi^{(\alpha)} = 1/2$ . The actual transition point  $\chi^{(\alpha)}$  depends on the line tension  $\lambda$  and attains the asymptotic value  $\chi^{(\alpha)} \approx 1/2$  in the limit of large  $\lambda$ .

The stability of vesicle morphologies with multiple  $\beta$  or liquid-disordered domains, as displayed in Fig. 3(a), can also be understood from the competition between the bending rigidities of the two domains and the line tension of the domain boundaries. When the number of the flexible  $\beta$  domains is increased, *e.g.*, from I<sub>1</sub> to I<sub>4</sub>, the rigid  $\alpha$  or liquid-ordered domain can attain a weakly curved state and lower its bending energy. The morphology II<sub>1</sub> has the largest line tension energy but the smallest bending energy because of the weakly curved  $\alpha$  domains. As long as the increase in line tension energy arising from an increased number of  $\beta$  domains does not exceed the decrease of bending energy, the morphologies with multiple  $\beta$  domains will be stable. For very large  $\kappa^{(\alpha)}/\kappa^{(\beta)}$ , the morphology II<sub>1</sub> is most favorable as mentioned before. The energy minimization in Fig. 3(b) shows qualitative agreement with the MC morphological transition I<sub>1</sub> → I<sub>2</sub> → I<sub>3</sub> → I<sub>4</sub> → II<sub>1</sub> as increasing bending rigidity ratio  $\kappa^{(\alpha)}/\kappa^{(\beta)}$ . Our explanation for the stability of the multi-domain morphologies based on the domain geometry is further confirmed by the energy decomposition in Fig. S3†, which shows that an increase in the number of  $\beta$  domains increases the line tension energy and reduces the bending energy, revealing that the morphologies with multiple  $\beta$  domains are stabilized by the reduction of bending energy.

For morphologies with multiple  $\beta$  or liquid-disordered domains such as I<sub>3</sub> and I<sub>4</sub> in Fig. 3(a), the flexible  $\beta$  domains can be strongly curved to shorten the length of the domain boundaries without leading to a large increase in the bending energy. For vesicles with small area fraction  $\chi^{(\alpha)}$ , for which the rigid  $\alpha$  or liquid-ordered phase represents the minority phase, we do not observe morphologies with more than two  $\alpha$  domains. Indeed, let us consider a vesicle with three or four  $\alpha$  domains. Since these

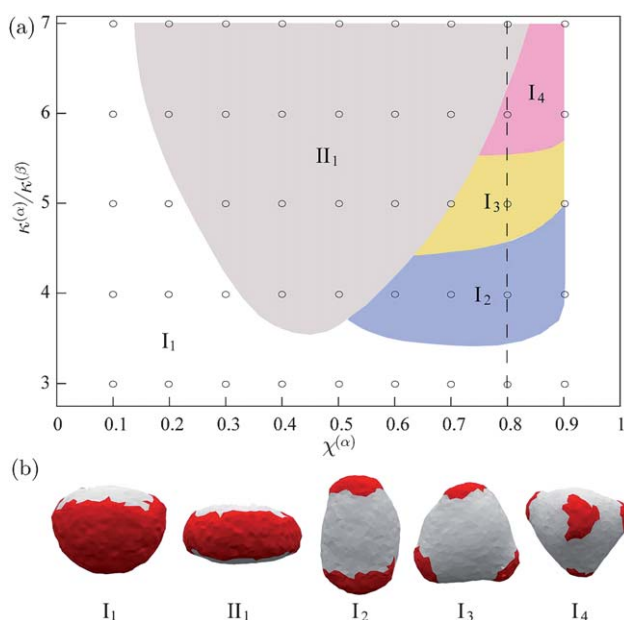


**Fig. 2** (a) Morphology diagram as a function of membrane composition  $\chi^{(\alpha)}$  and bending rigidity ratio  $\kappa^{(\alpha)}/\kappa^{(\beta)}$ , obtained from Monte Carlo simulations of vesicles that can freely adapt their volumes. The liquid-ordered  $\alpha$  phase is more rigid than the liquid-disordered  $\beta$  phase. Both the  $\alpha$  and the  $\beta$  domains have vanishing spontaneous curvature, and both domain types have equal Gaussian curvature moduli. The interaction parameter is  $U = 2U_c$  corresponding to the dimensionless line tension  $\lambda = 1.67$ , see eqn (24) and eqn (30). The open circles in the morphology diagram represent the parameter values for which simulations have been performed. The transition lines, which separate different morphologies indicated by different colors, are rough estimates and include those parameter values for which two stable morphologies have been observed. The vertical dashed line is related to Fig. 3. The notation for the morphologies is explained in the text. (b) Snapshots from the Monte Carlo simulations in (a). The liquid-ordered  $\alpha$  phase is shown in light grey and the liquid-disordered  $\beta$  phase in red.

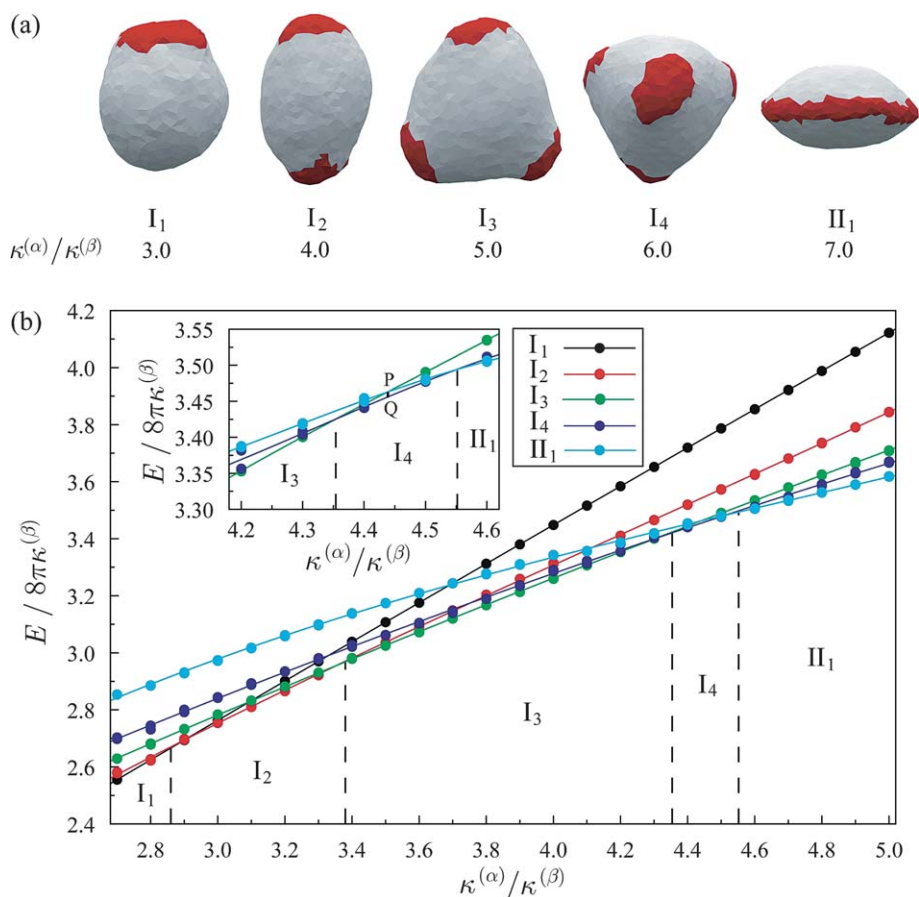


**Fig. 3** (a) Monte Carlo snapshots of vesicles for different bending rigidity ratios  $\kappa^{(\alpha)}/\kappa^{(\beta)}$  corresponding to the vertical dashed line in Fig. 2(a). The interaction parameter has the value  $U = 2U_c$  corresponding to the dimensionless line tension  $\lambda = 1.67$ , the area fraction  $\chi^{(\alpha)} = 0.8$ , and the vesicle volume is allowed to adapt freely. The  $\mathcal{L}_0$  or  $\alpha$  phase is shown in light grey and the  $\mathcal{L}_d$  or  $\beta$  phase in red. (b) Reduced total energy  $E/8\pi\kappa^{(\beta)}$  for vesicles with different morphologies as a function of  $\kappa^{(\alpha)}/\kappa^{(\beta)}$  as obtained from energy minimization. The parameters are the same as in (a). Solid lines in different colors are least-square fits of data points for different morphologies as indicated by the symbol legend. The inset shows the total energies for  $I_3$ ,  $I_4$  and  $II_1$  as a function of  $\kappa^{(\alpha)}/\kappa^{(\beta)}$ ; the morphology  $I_4$  is the lowest-energy state for  $4.35 \leq \kappa^{(\alpha)}/\kappa^{(\beta)} \leq 4.55$  with a maximal energy gap of  $\Delta E \approx 0.2\kappa^{(\beta)}$  indicated by the vertical line PQ. The ground states denoted by  $I_1$ ,  $I_2$ ,  $I_3$ ,  $I_4$  and  $II_1$  are separated by the vertical dashed lines, corresponding to the transition lines between these morphologies.

relatively rigid domains cannot bend easily to shorten the domain boundaries, the increase in line tension energy cannot be overcompensated by a reduction in bending energy. One might expect that the bending energy of the majority  $\beta$  phase could be reduced by having more  $\alpha$  domains, but this reduction in  $\beta$  bending energy is not sufficient in the absence of spontaneous curvature. In Sec. 3.3, we will show that the introduction of spontaneous curvature can stabilize such morphologies with multiple  $\alpha$  domains.

### 3.2 Effect of volume constraint

The volume of lipid vesicles is determined by osmotically active particles in the aqueous solution. Indeed, these vesicles adapt their volumes in such a way that the osmotic pressure inside the vesicles is balanced by the osmotic pressure in the exterior solution. In Fig. 4(a) and 4(b), we display morphology diagrams of vesicles with relatively large bending rigidity ratios as a function of membrane composition and reduced volume  $\nu$  as defined in eqn (27).

For  $\nu = 1$ , the vesicles attain spherical shapes and exhibit the morphology  $I_1$ , which minimizes the line tension energy. The reduced volume  $\nu$  represents a useful control parameter since it can be easily changed by osmotic deflation or inflation of the vesicles. If one starts with a spherical vesicle and decreases the reduced volume  $\nu$  for small values of the composition variable  $\chi^{(\alpha)}$ , the vesicle undergoes the morphological transition  $I_1 \rightarrow II_1$ , see Fig. 4(a) and 4(b). During this transition, both the rigid  $\alpha$  domain and the flexible  $\beta$  domain change their topologies: the large  $\alpha$  domain splits up into two smaller  $\alpha$  domains, which form two weakly curved caps, whereas the flexible  $\beta$  domain changes its topology from a cap to a narrow belt along the “equator” of the vesicle, see Fig. 3(a). For larger values of the composition variable  $\chi^{(\alpha)}$ , the vesicle attains additional morphologies such as  $I_3$  and  $I_4$  with more than two flexible  $\beta$  domains. It is interesting to note that, in the absence of a volume constraint, the corresponding parameter regions of the morphology diagram are mainly occupied by  $II_1$ , compare Fig. 2(a).

The multi-domain morphologies  $I_3$  and  $I_4$  have already been observed for lipid vesicles, see Fig. 1(b) and 1(d). Gudheti *et al.*<sup>13</sup>

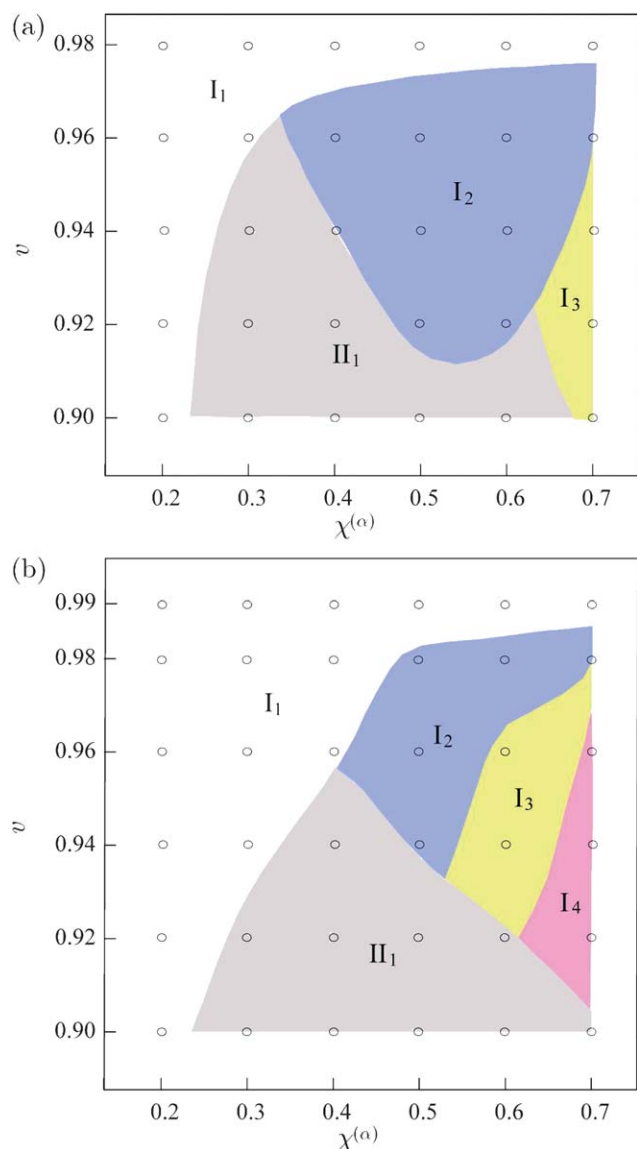


**Fig. 4** Morphology diagrams as a function of membrane composition  $\chi^{(\alpha)}$  and reduced volume  $\nu$  for interaction parameter  $U = 2U_c$ , corresponding to the dimensionless line tension  $\lambda = 1.67$ , and bending rigidity ratio (a)  $\kappa^{(\alpha)}/\kappa^{(\beta)} = 5.0$  or (b)  $\kappa^{(\alpha)}/\kappa^{(\beta)} = 6.0$ . The open circles, the morphologies  $I_n$  and  $II_1$ , as well as the transition lines separating different morphologies have the same meaning as in Fig. 2.

reported the  $I_3$  morphology for vesicles consisting of ESM/*trans*-DOPC/*cis*-DOPC/cholesterol for membrane composition  $\chi^{(\mathcal{L}_c)} = 0.57 \pm 0.09$  and bending rigidity ratio  $\kappa^{(\mathcal{L}_c)}/\kappa^{(\mathcal{L}_d)} \approx 5 \pm 1.56$ .<sup>6</sup> Veatch *et al.*<sup>11</sup> reported the  $I_4$  morphology for the vesicle of 1 : 1 DOPC/DMPC + 30% cholesterol, where the bending moduli of DOPC and DMPC + 30% cholesterol are  $23.1 \pm 3.5T^{32}$  and  $\sim 100 \pm 20T$ ,<sup>27</sup> respectively. Even though we do not know the exact membrane composition, the experimental observations agree quite well with our simulations for vesicles with volume constraint as shown in Fig. 1(a) and 1(c).

In addition to the parameter values shown in Fig. 4, we have also performed simulations of vesicles, for which the  $\alpha$  or liquid-ordered phase represented the minority phase and/or which were

characterized by smaller line tension such as  $U = 1.2U_c$ , smaller bending rigidity ratios  $3 \leq \kappa^{(\alpha)}/\kappa^{(\beta)} \leq 4$  and different reduced volumes. We did not observe morphologies such as  $III_1$  with more than two rigid  $\alpha$  domains.

### 3.3 Multi-domain morphologies induced by spontaneous curvature

In this subsection, we describe the effects of the spontaneous curvature of the different membrane domains on the multi-domain morphologies. In order to eliminate one parameter, no volume constraint will be taken into account here.

A spontaneous curvature of the more flexible  $\beta$  domains alone leads to the morphology diagram as shown in Fig. 5. For dimensionless spontaneous curvature  $m^{(\beta)}R_0 = 0$ , the morphologies in this figure are the same as those corresponding to the vertical dashed line in Fig. 2(a). For more negative spontaneous curvature, the vesicle exhibits morphologies with a smaller number of  $\beta$  domains; one example is provided by  $m^{(\beta)}R_0 = -1.0$  and  $\kappa^{(\alpha)}/\kappa^{(\beta)} = 5$  in Fig. 5, where the vesicle attains the  $I_2$  state with two  $\beta$  domains rather than the  $I_3$  state with three such domains. As the number of  $\beta$  domains is reduced from  $I_4$  to  $I_1$ , these domains become more weakly curved as previously shown in Fig. 3(a). In this way, the  $\beta$  domains are able to reduce their bending energy which would otherwise be increased by the negative value of the spontaneous curvature  $m^{(\beta)}R_0$ .

As one decreases the spontaneous curvature  $m^{(\beta)}R_0$  of the  $\beta$  domains towards negative values for large rigidity ratio  $\kappa^{(\alpha)}/\kappa^{(\beta)}$ , the vesicle undergoes a morphological transition from the  $II_1$  state with a single  $\beta$  domain to the  $I_4$  state with four  $\beta$  domains. In the  $II_1$  state, the flexible  $\beta$  phase forms one strongly curved domain around the “equator” sandwiched in between the two  $\alpha$  domains, see Fig. 3(a). As the spontaneous curvature of the

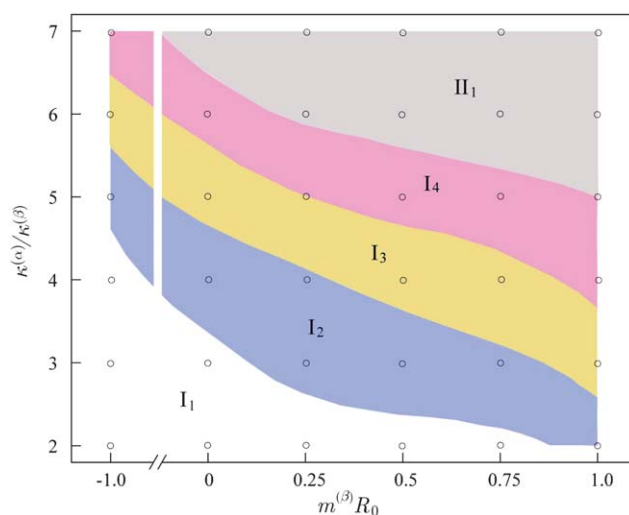


**Fig. 5** Morphology diagram as a function of dimensionless spontaneous curvature  $m^{(\beta)}R_0$  for the more flexible  $\beta$  phase and of bending rigidity ratio  $\kappa^{(\alpha)}/\kappa^{(\beta)}$  for vesicles with membrane composition  $\chi^{(\alpha)} = 0.8$ , interaction parameter  $U = 2U_c$  corresponding to line tension  $\lambda = 1.67$ , vanishing spontaneous curvature  $m^{(\alpha)} = 0$  of the more rigid  $\alpha$  phase, and no volume constraint. The open circles, the morphologies  $I_n$  and  $II_1$ , as well as the transition lines separating different morphologies have the same meaning as in Fig. 2.

$\beta$  domains is decreased towards negative values, this strongly curved  $\beta$  domain breaks up into four more weakly curved domains.

We also simulated vesicles, for which the more rigid  $\alpha$  domains had a nonzero spontaneous curvature. For  $m^{(\alpha)} < 0$ , the state  $\text{II}_1$  is most favorable for vesicles with a relatively large rigidity ratio  $\kappa^{(\alpha)}/\kappa^{(\beta)}$  because the two  $\alpha$  domains can then attain weakly curved shapes. For intermediate bending rigidity ratio, negative  $m^{(\alpha)}$  can also facilitate the formation of morphologies with more  $\beta$  domains since such a pattern reduces the curvature of the  $\alpha$  domain as shown in Fig. 3(a). For the vesicle with positive  $m^{(\alpha)}$ , the multi-domain morphology is not stable because the vesicle prefers  $\text{I}_1$  to minimize both the bending energy of the  $\alpha$  domain and the line tension energy.

For vesicles with minority  $\alpha$  or liquid-ordered phase, it is interesting to check whether the spontaneous curvature can stabilize those morphologies with multiple  $\alpha$  domains. Fig. 6 shows the spontaneous curvature effect on the morphology of a vesicle with minority  $\alpha$  phase for different values of the interaction parameter  $U$ . As illustrated in Fig. 6(b), for  $m^{(\alpha)}R_0 = -1.0$ , the vesicle assumes the oblate  $\text{II}_1$  morphology, where the two

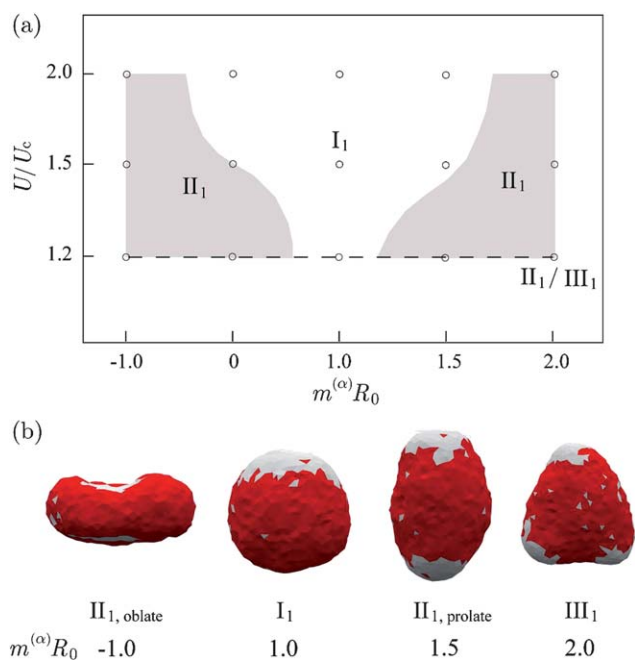


**Fig. 6** (a) Morphology diagram as a function of dimensionless interaction parameter  $U/U_c$  and dimensionless spontaneous curvature  $m^{(\alpha)}R_0$ . The liquid-ordered  $\alpha$  phase represents the minority phase. The vesicle membrane has composition  $\chi^{(\alpha)} = 0.2$ , bending rigidity ratio  $\kappa^{(\alpha)}/\kappa^{(\beta)} = 4.0$ ,  $m^{(\beta)}R_0 = 0$  and experiences no volume constraint. The open circles and the transition lines separating different morphologies have the same meaning as in Fig. 2. For  $(m^{(\alpha)}R_0, U/U_c) = (2.0, 1.2)$ , the vesicle adopts both  $\text{II}_1$  and  $\text{III}_1$  as stable morphologies with the average reduced volumes  $0.86 \pm 0.01$  and  $0.87 \pm 0.01$ , respectively. The spacings on the  $x$ - and  $y$ -axes are nonuniform. (b) Monte Carlo snapshots for vesicles simulated along the horizontal dash line in (a) with  $U = 1.2U_c$ . The liquid-disordered  $\beta$  phase is shown in red and the liquid-ordered  $\alpha$  phase in light grey. For the oblate shape  $\text{II}_{1,\text{oblate}}$  and the prolate shape  $\text{II}_{1,\text{prolate}}$ , the two rigid  $\alpha$  domains curve towards the vesicle interior and exterior, respectively.

separate  $\alpha$  domains curve towards the interior compartment in order to minimize the bending energy. For  $m^{(\alpha)}R_0 = 1.0$ , the  $\alpha$  phase prefers to curve towards the exterior compartment and therefore  $\text{I}_1$  is most favorable both with respect to the bending energy and to the line energy. For relatively small line tensions corresponding to interaction parameters such as  $U = 1.2U_c$ , the vesicle can form the prolate morphology  $\text{II}_1$  and even  $\text{III}_1$  with up to three  $\alpha$  domains when increasing  $m^{(\alpha)}$ . Thus, the increase in line energy arising from an increased number of domains can be compensated by the decrease in the bending energy arising from a decreased difference between the actual curvature and the spontaneous curvature of the  $\alpha$  domains. For  $U = 1.5U_c$  and  $U = 2U_c$ , the larger line tensions disfavor the formation of the  $\text{II}_1$  and  $\text{III}_1$  morphologies unless the spontaneous curvature  $m^{(\alpha)}$  is sufficiently large. If the absolute value of  $m^{(\alpha)}$  exceeds  $|m^{(\alpha)}| = 1/R_0$ , the rigid  $\alpha$  domains will start to bud off from the majority  $\beta$  phase.

### 3.4 Multiple $\mathcal{L}_d$ domains stabilized by Gaussian curvature

Finally, we address the dependence of the vesicle morphologies on the Gaussian curvature moduli  $\kappa_G^{(\alpha)}$  and  $\kappa_G^{(\beta)}$ . Because of the Gauss–Bonnet theorem, these morphologies depend only on the difference or contrast  $\Delta\kappa_G = \kappa_G^{(\alpha)} - \kappa_G^{(\beta)}$  as defined in eqn (29). Furthermore, we will again use the bending rigidity  $\kappa^{(\beta)}$  as the basic energy scale and compare different values for the dimensionless contrast  $\Delta\kappa_G/\kappa^{(\beta)}$ .

In Fig. 7(a), we display the morphology diagram of vesicles with composition  $\chi^{(\alpha)} > 1/2$  and contrast  $\Delta\kappa_G/\kappa^{(\beta)} = 0.8$ . The corresponding morphology diagram for vanishing  $\Delta\kappa_G$  is shown in Fig. 7(b) for comparison. It is evident here that the

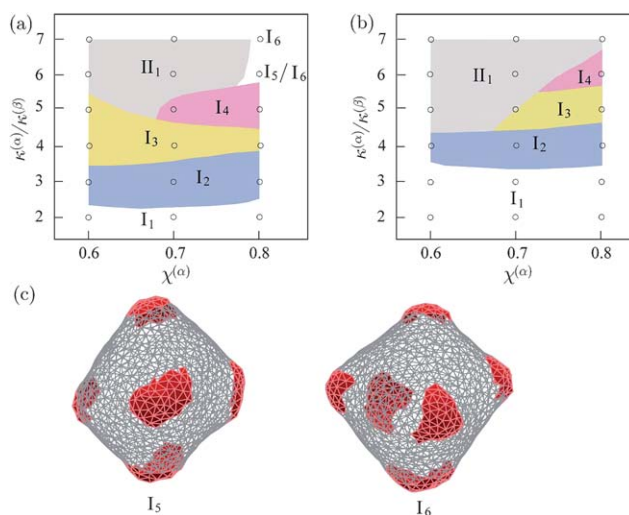


**Fig. 7** Morphology diagrams depending on membrane composition  $\chi^{(\alpha)}$  and bending rigidity ratio  $\kappa^{(\alpha)}/\kappa^{(\beta)}$  for (a)  $\Delta\kappa_G/\kappa^{(\beta)} = 0.8$  and (b)  $\Delta\kappa_G/\kappa^{(\beta)} = 0$ . The vesicles can freely adapt their volumes. The interaction parameter is  $U = 2U_c$  corresponding to the dimensionless line tension  $\lambda = 1.67$ . The notation  $\text{I}_5/\text{I}_6$  for  $(\chi^{(\alpha)}, \Delta\kappa_G/\kappa^{(\beta)}) = (0.8, 6)$  in (a) indicates that the two morphologies  $\text{I}_5$  and  $\text{I}_6$  are both (meta)stable for the same vesicle. (c) Monte Carlo snapshots of the morphologies  $\text{I}_5$  and  $\text{I}_6$  in (a). The flexible liquid-disordered  $\beta$  domains are red, the rigid liquid-ordered  $\alpha$  domain is made transparent. The average reduced volumes for the morphologies  $\text{I}_5$  and  $\text{I}_6$  are  $v = 0.90 \pm 0.01$  and  $v = 0.89 \pm 0.01$ , respectively.

introduction of positive  $\Delta\kappa_G$  promotes the formation of morphologies with multiple  $\beta$  or liquid-disordered domains. For example, the vesicle adopts  $I_2$  for  $\Delta\kappa_G/\kappa^{(\beta)} = 0$  and  $I_3$  for  $\Delta\kappa_G/\kappa^{(\beta)} = 0.8$  with  $\chi^{(\alpha)} = 0.6$ ,  $\kappa^{(\alpha)}/\kappa^{(\beta)} = 4$ . For the vesicle with  $\chi^{(\alpha)} = 0.8$ , one can even have  $I_5$  and  $I_6$  morphologies for  $\kappa^{(\alpha)}/\kappa^{(\beta)} = 6$  and  $\kappa^{(\alpha)}/\kappa^{(\beta)} = 7$ , as in the snapshots of Fig. 7(c). As shown in Fig. 7(c) as well as Fig. 3(a), the flexible  $\beta$  domains are more strongly curved than the rigid  $\alpha$  or liquid-ordered domains. This implies that the Gaussian curvature of the  $\beta$  domains is more positive than the one of the  $\alpha$  domains since the  $\beta$  domains curve outwards. Therefore, such morphologies with multiple  $\beta$  domains are stabilized by more negative  $\kappa_G^{(\beta)}$ . In other words, the decrease in bending energy of the vesicle by having  $\Delta\kappa_G > 0$  can help the vesicle develop even more  $\beta$  domains.

By analogy, one might expect that morphologies with multiple rigid  $\alpha$  or liquid-ordered domains could also be stabilized for membrane composition  $\chi^{(\alpha)} < 1/2$  if the Gaussian curvature modulus of the rigid  $\alpha$  phase attains a more negative value. We simulated such vesicles for different line tensions but did not observe such a stabilization and, thus, were not able to stabilize the morphology  $III_1$ , compare to Fig. 6(b), by only increasing the contrast of the Gaussian curvature moduli.

## 4 Conclusion

We have studied the morphologies of thermally fluctuating vesicles with coexisting  $\alpha$  and  $\beta$  or liquid-ordered and liquid-disordered domains by extensive Monte Carlo simulations. In order to understand how the competition between the bending energies of the domains and the line tension energy of the domain boundaries determines the domain patterns, we constructed the morphology diagrams of the vesicles as a function of membrane composition  $\chi^{(\alpha)}$  as defined by eqn (28) and of bending rigidity ratio  $\kappa^{(\alpha)}/\kappa^{(\beta)}$ , as shown in Fig. 2.

If the majority phase was provided by the  $\alpha$  or liquid-ordered phase, we found stable morphologies of vesicles consisting of a single  $\alpha$  domain with three or four  $\beta$  or liquid-disordered domains, see the MC snapshots in Fig. 1(a) and 1(c). Multi-domain morphologies with three and four liquid-disordered domains have also been observed experimentally by optical microscopy,<sup>11,13</sup> the corresponding images agree quite well with our simulation snapshots, see Fig. 1(b) and 1(d). For these morphologies, the more flexible liquid-disordered domains have a relatively large curvature which allows the more rigid liquid-ordered domain to bend only weakly in order to lower the bending energy. At the same time, the length of the domain boundaries does not increase substantially to destabilize such multi-domain patterns. Energy minimization as in Fig. 3(b) also shows that the vesicles can have stable morphologies with multiple liquid-disordered domains as one increases the bending rigidity ratio  $\kappa^{(\alpha)}/\kappa^{(\beta)}$ , which is consistent with the MC findings shown in Fig. 3(a). The energy decomposition displayed in Fig. S3† further supports our explanation for the stability of the multi-domain morphologies.

In addition to the bending rigidities of the membrane domains and the line tension of the domain boundaries, other system parameters such as spontaneous curvatures, constraints on the vesicle volume, and differences in the Gaussian curvature moduli can facilitate the formation of such morphologies with multiple

$\beta$  or liquid-disordered domains as demonstrated in Secs. 3.2–3.4. In particular, novel morphologies with a stable pattern of up to six  $\beta$  domains were found if the two domains had different Gaussian curvature moduli, see Fig. 7(c). One important conclusion from our study is that these morphologies are even stable in the presence of thermally-excited fluctuations that perturb both the vesicle shapes and the domain patterns.

If the majority phase was provided by the  $\beta$  or liquid-disordered phase, we also observed morphologies with multiple rigid  $\alpha$  or liquid-ordered domains for small line tensions and relatively large spontaneous curvatures of the liquid-ordered phase, see the  $II_1$  and  $III_1$  morphologies in Fig. 6(b). One open question regarding these morphologies with multiple liquid-ordered domains or “lipid rafts” is to what extent these morphologies may represent stable equilibrium states. Our simulations indicate that such patterns of liquid-ordered domains can be stable for relatively large spontaneous curvatures of these domains and relatively small line tensions of the domain boundaries.

In our simulations, the material parameters of the membranes, such as the bending rigidities of the membrane domains and the differences in the Gaussian curvature moduli, were chosen in accordance with experimental values, see the ESI†. Therefore, the different multi-domain morphologies should also be accessible to experiment. Indeed, two of these morphologies, namely  $I_3$  and  $I_4$  have already been observed, see Fig. 1, but a systematic exploration of the morphology diagrams has not been pursued so far. Presumably the simplest way to explore these morphologies experimentally would be by changing the vesicle volume *via* osmotic deflation or inflation. Indeed, as shown in Fig. 4, the vesicles can attain five different multi-domain morphologies as a function of membrane composition  $\chi^{(\alpha)}$  and reduced volume  $v$ . For membrane composition  $0.4 \leq \chi^{(\alpha)} \leq 0.5$ , deflation of a spherical vesicle should lead to three different multi-domain morphologies corresponding to the sequence  $I_1 \rightarrow I_2 \rightarrow II_1$ , which involves two morphological transitions. During the transition  $I_1 \rightarrow I_2$ , the liquid-disordered domain splits up into two such domains. During the transition  $I_2 \rightarrow II_1$ , the domain pattern is inverted which strongly affects the vesicle shape, see Fig. 3(a). For membrane composition  $0.65 \leq \chi^{(\alpha)} \leq 0.7$ , deflation of a spherical vesicle can lead to the extended sequence  $I_1 \rightarrow I_2 \rightarrow I_3 \rightarrow I_4 \rightarrow II_1$ , which involves even four morphological transitions. All of these transitions change the topology of the stable domain patterns, a transformation that should be easy to detect in the fluorescence microscope.

## References

- 1 J. Rowlinson and B. Widom, *Molecular Theory of Capillarity*, Clarendon Press, Oxford, 1989.
- 2 R. Lipowsky, *J. Phys. II*, 1992, **2**, 1825–1840.
- 3 F. Jülicher and R. Lipowsky, *Phys. Rev. Lett.*, 1993, **70**, 2964–2967.
- 4 T. Baumgart, S. Hess and W. Webb, *Nature*, 2003, **425**, 821–824.
- 5 K. Bacia, P. Schwille and T. Kurzchalia, *Proc. Natl. Acad. Sci. U. S. A.*, 2005, **102**, 3272–3277.
- 6 T. Baumgart, S. Das, W. W. Webb and J. T. Jenkins, *Biophys. J.*, 2005, **89**, 1067–1080.
- 7 R. Dimova, K. A. Riske, S. Aranda, N. Bezlyepkina, R. L. Knorr and R. Lipowsky, *Soft Matter*, 2007, **3**, 817–827.
- 8 S. Semrau, T. Idema, L. Holtzer, T. Schmidt and C. Storm, *Phys. Rev. Lett.*, 2008, **100**, 088101.
- 9 K. Simons and E. Ikonen, *Nature*, 1997, **387**, 569–572.

- 10 S. Kumar, G. Gompper and R. Lipowsky, *Phys. Rev. Lett.*, 2001, **86**, 3911–3914.
- 11 S. L. Veatch and S. L. Keller, *Biophys. J.*, 2003, **85**, 3074–3083.
- 12 E. Gutleiderer, T. Gruhn and R. Lipowsky, *Soft Matter*, 2009, **5**, 3303–3311.
- 13 M. V. Gudheti, M. Mlodzianoski and S. T. Hess, *Biophys. J.*, 2007, **93**, 2011–2023.
- 14 F. Jülicher and R. Lipowsky, *Phys. Rev. E: Stat. Phys., Plasmas, Fluids, Relat. Interdiscip. Top.*, 1996, **53**, 2670–2683.
- 15 W. Rawicz, K. C. Olbrich, T. McIntosh, D. Needham and E. Evans, *Biophys. J.*, 2000, **79**, 328–339.
- 16 W. Helfrich, *Z. Naturforsch. C*, 1973, **28**, 693–703.
- 17 M. do Carmo, *Differential Geometry of Curves and Surfaces*, Prentice Hall, 1976.
- 18 R. Goetz, G. Gompper and R. Lipowsky, *Phys. Rev. Lett.*, 1999, **82**, 221–224.
- 19 P. S. Kumar and M. Rao, *Mol. Cryst. Liq. Cryst.*, 1996, **288**, 105–118.
- 20 F. Jülicher, Ph.D. Thesis, Universität zu Köln, 1994.
- 21 M. Meyer, M. Desbrun, P. Schröder and A. H. Barr, in *Discrete differential-geometry operators for triangulated 2-manifolds*, ed. H.-C. Hege and K. Polthier, Springer-Verlag, Berlin, 2003, pp. 35–57.
- 22 E. Akleman and J. Chen, in *Insight for Practical Subdivision Modeling with Discrete Gauss-Bonnet Theorem*, ed. M.-S. Kim and K. Shimada, Springer-Verlag, Berlin, 2006, pp. 287–298.
- 23 D. S. Richeson, *Euler's Gem: The Polyhedron Formula and the Birth of Topology*, Princeton University Press, 2008.
- 24 R. M. F. Houtappel, *Physica*, 1950, **16**, 425–455.
- 25 R. R. Netz and P. Pincus, *Phys. Rev. E: Stat. Phys., Plasmas, Fluids, Relat. Interdiscip. Top.*, 1995, **52**, 4114–4128.
- 26 T. R. Weikl, *Europhys. Lett.*, 2001, **54**, 547–553.
- 27 U. Seifert and R. Lipowsky, in *Structure and Dynamics of Membranes*, ed. R. Lipowsky and E. Sackmann, Elsevier, Amsterdam, 1995, ch. 8, pp. 403–462.
- 28 U. Seifert, *Adv. Phys.*, 1997, **46**, 13–139.
- 29 T. Gruhn, T. Franke, R. Dimova and R. Lipowsky, *Langmuir*, 2007, **23**, 5423–5429.
- 30 N. Akutsu and Y. Akutsu, *J. Phys. A: Math. Gen.*, 1990, **23**, L217–222.
- 31 K. Brakke, *Exp. Math.*, 1992, **1**, 141–165.
- 32 N. Fa, L. Lins, P. Courtoy, Y. Dufrêne, P. V. D. Smissen, R. Brasseur, D. Tyteca and M.-P. Mingeot-Leclercq, *Biochim. Biophys. Acta, Biomembr.*, 2007, **1768**, 1830–1838.